

3D NUMERICAL MODELS FOR ALONG-AXIS VARIATIONS IN DIKING AT  
MID-OCEAN RIDGES

by

Xiaochuan Tian

A Thesis

Submitted in Partial Fulfillment of the  
Requirements for the Degree of  
Master of Science

Major: Geophysics

The University of Memphis

May, 2015

Copyright © 2015 Xiaochuan Tian

All rights reserved

### ***Dedication***

I would like to dedicate this Thesis to my mother, Xia Tian, the most important person in my life. Without her guidance and support, I will not become who I am.

*Acknowledgements*

To Eunseo,  
To Committee members,  
To CERI,

### *Abstract*

Tian, Xiaochuan. M.S. The University of Memphis. May 2015. 3D Numerical Models for Along-axis Variations in Diking at Mid-Ocean Ridges. Major Professor: Eunseo Choi.

Bathymetry of ocean floors reveals a great variety of morphologies at Mid-ocean Ridges (MORs). Previous studies showed that the morphologies at slow spreading MORs are mainly controlled by the ratio between rates of magma supply and plate extension. 2D models for the across-ridge cross-sections have been successful in explaining many of the observed morphological features such as abyssal hills and oceanic core complexes. However, the magma supply varies along the ridge and the interaction between the tectonic plates and magmatism at MORs are inevitably 3D processes. We propose to investigate the consequences of the along-axis variability in diking in terms of faulting pattern and the associated structures. This work will include implementation of an algorithm of parameterizing repeated diking in a 3D parallel geodynamic modeling code.

*Table of Contents*

Chapter	Page
<b>1 Introduction</b>	<b>1</b>
1.1 Research Questions . . . . .	1
1.2 Review of Literature . . . . .	1
1.3 Statement of Research Purpose . . . . .	5
1.4 Findings . . . . .	6
<b>2 Methods</b>	<b>7</b>
2.1 Method of approach . . . . .	7
2.2 Model Setup . . . . .	9
2.3 Parameters to control . . . . .	9
<b>3 Results</b>	<b>11</b>
3.1 Reference model description . . . . .	11
3.1.1 M varies along the ridge axis . . . . .	12
3.1.2 Constant M along the ridge axis . . . . .	14
3.2 Tables of all the data points . . . . .	15
3.3 Fault Alternation . . . . .	17
3.4 Variation of the range of M . . . . .	17
3.5 Variation of the functional form . . . . .	17
3.6 Influence of weakening rate . . . . .	17
3.7 Summary of Findings . . . . .	17
<b>4 Discussion</b>	<b>18</b>
4.1 Discussion of Findings . . . . .	18
4.2 Influence of healing . . . . .	18
4.3 Model Limitation . . . . .	18

4.4	Reccommendation for Future Research . . . . .	18
<b>5</b>	<b>Conclusions</b>	<b>19</b>

# **1 Introduction**

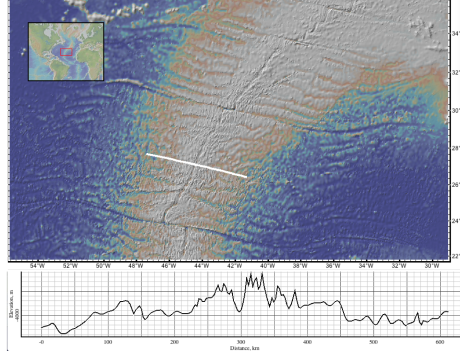
Around 70% of the Earth's crust is oceanic crust and the mid-ocean ridges (MORs), the longest mountain chains on the Earth, are where new crust are forming with a multitude of seismic and volcanic activities. To study how new crust is created and how MORs evolve is significant for Earth Sciences. Geodynamic modeling along with a variety of geological, geophysical observation and lab experiment constraints have been used to study how the MORs work as a system under geological time scale.

## **1.1 Research Questions**

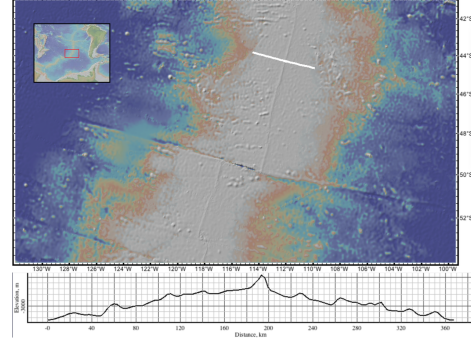
High-resolution multi-beam bathymetry has revealed various characteristics of topography along and across MOR axis. Three specific questions stimulate people's interests most. First, what causes the distinct difference in axial topography between slow and fast spreading ridges. Second, for slow spreading ridges, why does topography along ridge varies and how to explain many features observed. Third, why do oceanic core complexes (OCCs) form and what is the mechanism.

## **1.2 Review of Literature**

According to [Fowler, 2004], variations in mid-ocean ridge morphologies are mainly controlled by four factors: magma supply, tectonic strain, hydrothermal circulation and spreading rate. Among them, the spreading rate is the most important. Slow-to-intermediate spreading centers (half spreading rate less than 4cm/year) produce median valleys that are typically 10~20km wide and 1~2km deep (e.g., Mid-Atlantic Ridges, Figure 1(a)). Fast-spreading centers (half spreading rate greater than 5cm/year) have axial highs that are 10~20 km wide, 0.3~0.5 km high (e.g., East Pacific Rise, Figure 1(b)).



(a) Slow spreading Mid-Atlantic Ridge



(b) Fast spreading East Pacific Rise

Figure 1: Profiles of bathymetry across MORs.

Slow spreading ridges exhibit along-axis variations as well in terms of the width and depth of median valleys and the off-axis morphology. Figure 2 shows that the topographic profile nearer to the center of the ridge segment (A-A') is rather symmetric and has higher frequency. The maximum relief is about 1km. In contrast, the near-tip profile (B-B') is asymmetric and has much lower frequency and a greater relief ( $\sim 3$ km). The bathymetry and crustal thickness along the ridge valley also varies. From [Chen and Lin, 1999], the maximum along-axis variation in crustal thickness  $\Delta H_c$  is linearly increasing with segment length  $L$ , and the relationship is  $\Delta H_c(L) = 0.0206L$  (Figure 3).

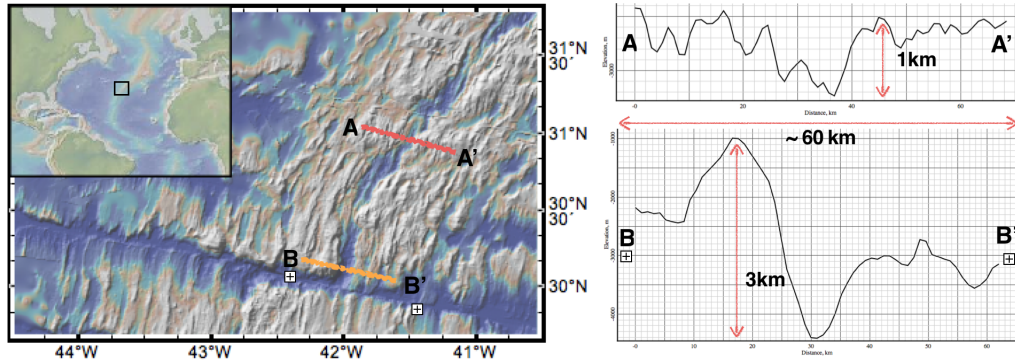


Figure 2: Two bathymetry cross-sections of Mid-Atlantic Ridge (MAR) with 10 times vertical exaggeration. A-A' is closer to the ridge segment center while B-B' is at the tip of the segment near the Atlantis Transform fault.

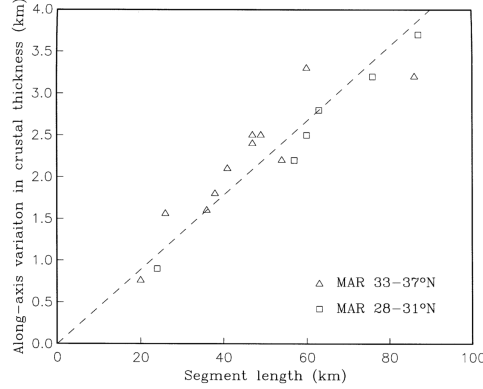


Figure 3: Relationship between the maximum crustal thickness variations along a ridge segment and the segment length. The dashed line is the best-fit linear regression of the combined data. [Chen and Lin, 1999]

Magma supply at MORs is mostly a passive process when no hot plume presents [Fowler, 2004]. Hot mantle rises up to fill the vacated room being created by plate separation and decompression will lead to partial melting of the hot mantle. The melt upwells due to both pressure difference and buoyancy from lateral density difference. When the melt solidifies near the surface, it forms new crust. This diking process can also release extensional stresses result from far-field driving forces.

The passive nature of magma supply results in the major difference between fast and slow spreading ridges in the amount of magma supply. At the fast spreading ridges, magma supply is always sufficient for accommodating plate separation by filling the space by dikes. However, the amount of magma supplied in the form of dikes is not as much at slow spreading ridges and the oceanic lithosphere experiences internal deformations (i.e. tectonics process like normal faulting) when the accumulated extensional stress exceeds the strength of the crust.

Buck et al. [2005] attributed the contrasting faulting patterns and ocean floor morphology of fast- and slow-spreading ridges to the difference in the amount of plate extension accommodated by diking. They defined the ratio between the rates of diking and plate separation as  $M = V_{dx}/2V_x$ , where  $V_{dx}$  is the extensional velocity of a widening dike and  $V_x$  is the half spreading rate of the MOR. According to this definition,  $M = 1$  represents the case

where diking is frequent enough to release all the tensional stresses from plate separation.  $M = 0$  corresponds to the case of no magma supply, in which diking does not account for any of the plate motion and therefore plates kinematics requires plates to go through internal deformations. As shown in Figure 4, an axial high forms at a fast spreading ridge ( $M=1$ ) due to buoyancy from lateral density difference across ridge axis but a median valley forms at a slow-spreading ridge ( $M=0.5$ ) due to near-axis normal faulting, which is in turn caused by the stretching of oceanic lithosphere.

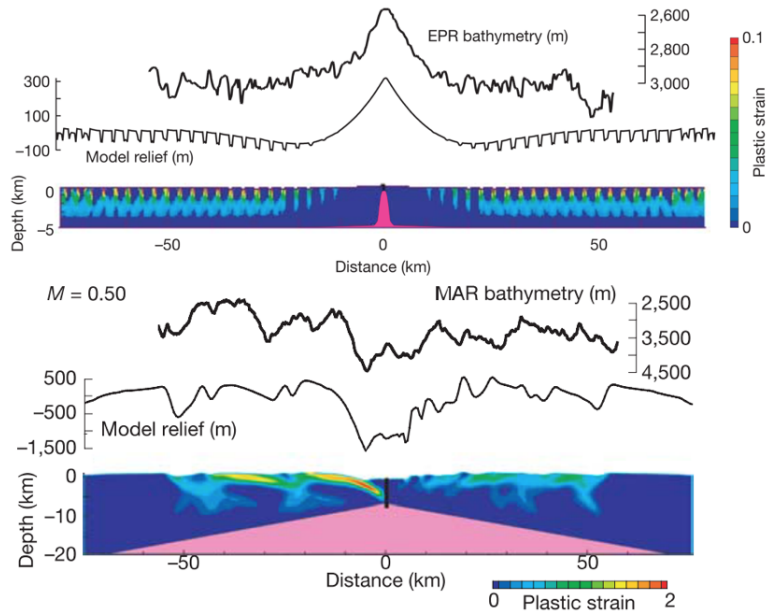


Figure 4: Upper one: modeling result for fast spreading agrees well with the observation of East Pacific Rise. Lower one: modeling result for slow spreading ridges agrees well with the bathymetry of Mid Atlantic Ridge. [Buck et al., 2005]

Tucholke et al. [2008] expanded the investigation on the role of  $M$  in the mid-ocean ridge mechanics. They focused on faulting behaviors of slow spreading ridges and find that the OCCs are most likely to form when  $M$  varies from 0.3 to 0.5. As shown in Figure 5, when  $M=0.7$ , repeated diking pushes faults forming at the spreading center away from axis. Since the thickness of the brittle layer increases away from the ridge axis, frictional and bending energy for maintaining the fault also increases. When it exceeds the energy for breaking a new near-axis fault, the old fault will be replaced by the new one. When

$M=0.3\sim0.5$ , the normal faults remains active for a long time to become detachment faults, exhuming the lower crust and mantle materials to the seafloor. When  $M$  is less than 0.3, most of the tension is accommodated by intra-plate deformations rather than by diking and as a result, faulting pattern is more complicated and unsteady.

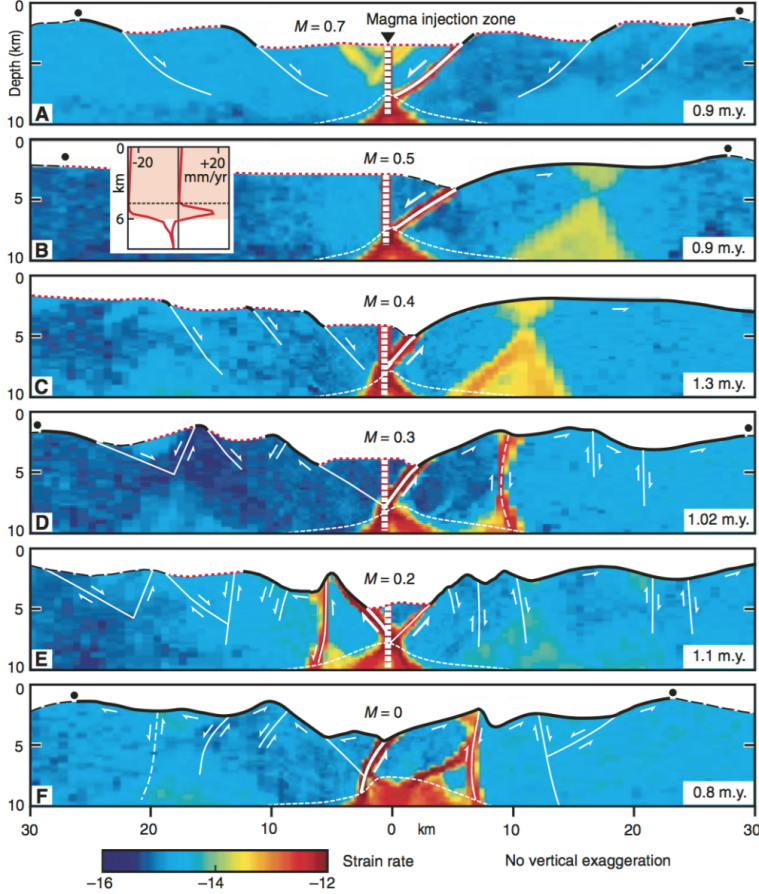


Figure 5: A~F: Faulting behavior for different values of  $M$ . Geologic interpretation is superimposed on modeled distribution of strain rate. Dots show breakaways of initial faults. Dashed seafloor is original model seafloor, red dotted seafloor is formed dominantly by magmatic accretion, and solid bold is fault surface. Note that detachment faults in B and C are not interrupted by secondary faults. [Tucholke et al., 2008]

### 1.3 Statement of Research Purpose

The  $M$ -factor formulation used in these previous 2D models successfully explained major features found in across-ridge profiles of seafloor bathymetry. However, 2D models have limitations in studying the along ridge-axis interactions, especially when important variables are not constant along the ridge axis. Magma supply at fast spreading ridges seems always sufficient for accommodating plate motions with little variation along the ridge axis. The relatively uniform topography along fast spreading ridges is considered to be consis-

tent with the uniformly abundance of magma supply. However, along the slow spreading ridges, bathymetry, gravity anomaly and results from reflection and refraction seismology show good correlation with variation in crustal thickness [Ryan et al., 2009, Chen and Lin, 1999, Lin et al., 1990, Tolstoy et al., 1993]. Because oceanic crust is mainly formed by upwelled magma at the ridge, variation in the thickness of the crust implies variation in magma supply. At slow spreading ridges, hydrothermal cooling, thermal structures and even local spreading rate [Baines et al., 2008] also varies both along and across the ridge axis and they appear interrelated. Thus, for slow-to-intermediate spreading ridges, the interactions between tectonics and magmatism at MORs are inevitably 3D processes and 3D numerical models are desirable for better understanding factors controlling both across-and along-ridge variations.

## 1.4 Findings

## 2 Methods

The purpose of this thesis is to study how the along-ridge variation in M will make a contribution to the observed various topography assuming that M is the first order control over the topography evolution of MORs governing the interaction between magmatism and tectonic deformations. We will extend the M-factor formulation originally developed for 2D models to 3D by implementing it into a 3D numerical modeling code SNAC [Choi et al., 2008]. We will focus on studying the last two questions mentioned in the introduction: 1) why does topography along ridge varies and how to explain many features observed; 2) why do OCCs form and what is the mechanism.

By systematically exploring the behaviors of the 3D models and comparing them with observations, we will be able to better understand how the mid-ocean ridge magmatism and tectonic deformations interact.

### 2.1 Method of approach

The numerical modeling code, SNAC, is an explicit Lagrangian finite element code. It solves the force balance equation for elasto-visco-plastic materials. Figure 6 shows major parts of the SNAC's algorithm.

For each time step  $dt$ , strain and strain rates are updated based on the boundary conditions shown in Figure 7. A constitutive model returns updated stresses corresponding to these deformation measures. Internal forces are then calculated from the update stresses, which is plugged into the momentum balance equation together with the body force term. Then, the net force divided by internal mass yields acceleration at a node point, which is time-integrated to velocity and displacement.

A 3D domain is discretized into hexahedral elements, each of which is in turn divided into two sets of tetrahedra. This symmetric discretization prevents faulting from favoring a specific direction or “mesh grains”.

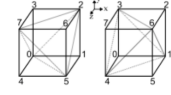
Rheology for the oceanic lithosphere is assumed to be elasto-visco-plastic. When viscosity is high at low temperature, the rheology essentially becomes the Mohr-Coulomb plasticity with strain softening and thus can create shear bands that behave like faults. Strain softening is realized by cohesion decreasing with increasing amount of permanent (i.e., plastic) strain. We assume this relationship is linear for simplicity such that it is sufficient for a full description of strain weakening to define initial and final values of cohesion and a critical plastic strain at which cohesion becomes the final value. We define the rate of strain weakening as the cohesion difference divided by the critical plastic strain and use it as one of the model parameters. When temperature is high and viscosity is low, the rheology becomes the Maxwell viscoelasticity and can model creeping flow. By assuming an appropriate initial temperature distribution, we can effectively set up a structure of a brittle lithosphere and a ductile asthenosphere. Rheological parameters are taken from previous studies that used a similar rheology [Buck 2005; Tuckholke et al., 2008] or from lab experiments [e.g., Kirby and Kronenberg, 1987].

For 3D diking processss, the expanding strain  $\Delta\varepsilon_{xx}$  results from diking at the ridge will lead to extra-stresses in all three directions  $\Delta\sigma_{xx}$ ,  $\Delta\sigma_{yy}$  and  $\Delta\sigma_{zz}$  based on the constitutive equations  $\sigma_{ij} = \delta_{ij}\lambda\varepsilon_{ij} + 2\mu\varepsilon_{ij}$ .

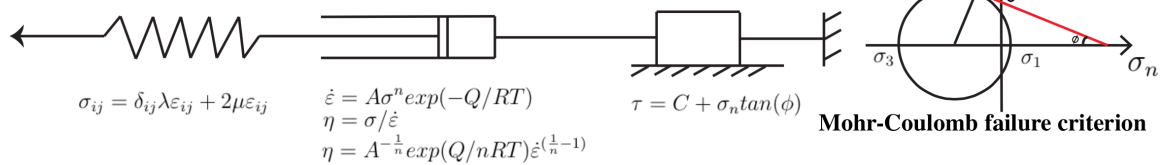
**SNAC:** a 3D, MPI parallelized, updated Lagrangian explicit finite difference code for modeling long-term tec-tonic evolution of the Earth's elasto-visco-plastic crust and mantle. (Choi et al., 2008)

**Momentum Balance Equation:**  $\frac{\partial\sigma_{ij}}{\partial x_j} + \rho g_i = \rho \frac{Dv_i}{Dt}$

**Spatial Decritization:** A 3D domain is discretized into hexahedral elements, each of which is filled with two sets of 5 tetrahedra.



**Elasto-Visco-Plastic (EVP) Rheology:**



**Diking M Formulation:**  $\text{M= } Vdx / 2Vx$  (Vdx is the dike accretion strain(dike widening) $\Delta\varepsilon_{xx}$  in each time step dt)

Stresses introduced by a dike accretion strain(dike widening) $\Delta\varepsilon_{xx}$  in each time step dt:

$$\Delta\sigma_{xx} = (\lambda + 2\mu)\Delta\varepsilon_{xx} \quad \Delta\sigma_{yy} = \lambda\Delta\varepsilon_{xx} \quad \Delta\sigma_{zz} = \lambda\Delta\varepsilon_{xx}$$

Figure 6: Essential components of the numerical method to be used for the proposed research

## 2.2 Model Setup

<sup>XT:</sup> Add a table for parameters in use. The 3D models has a geometry of  $(60\text{km} \times 20\text{km} \times 20\text{km})$  in X, Y and Z axes respectively with a resolution of  $\text{dx} = 1\text{km}$  ( $\text{dx}$  is the length scale for each hexahedron element). For pseudo-2D models, they have a geometry of  $(60\text{km} \times 20\text{km} \times 1\text{km})$  in X, Y and Z axes respectively with a resolution of  $\text{dx} = 0.5\text{km}$ . As shown in Figure 7, temperature linearly increases from  $0^\circ\text{C}$  at the top surface to  $240^\circ\text{C}$  at the depth of 6 km, reflecting enhanced cooling due to hydrothermal circulation. Below 6 km, the temperature profile follows the semi-infinite half-space cooling model of moving plates [e.g., Turcotte and Schubert, 2002]. Two sides perpendicular to the  $z$  coordinate axis are free-slip. The top surface has a vertical traction from water column, of which height is locally determined as  $4000 - h(x,z)$  m, where  $h(x,z)$  is the topography at a location,  $(x,z)$ . The bottom surface is supported by the Winkler foundation. Temperature is fixed at  $0^\circ\text{C}$  on the top surface and at  $1300^\circ\text{C}$  on the bottom surface. We will adopt the power-law rheology of dry diabase[e.g., Kirby and Kronenberg, 1987, Buck et al., 2005].

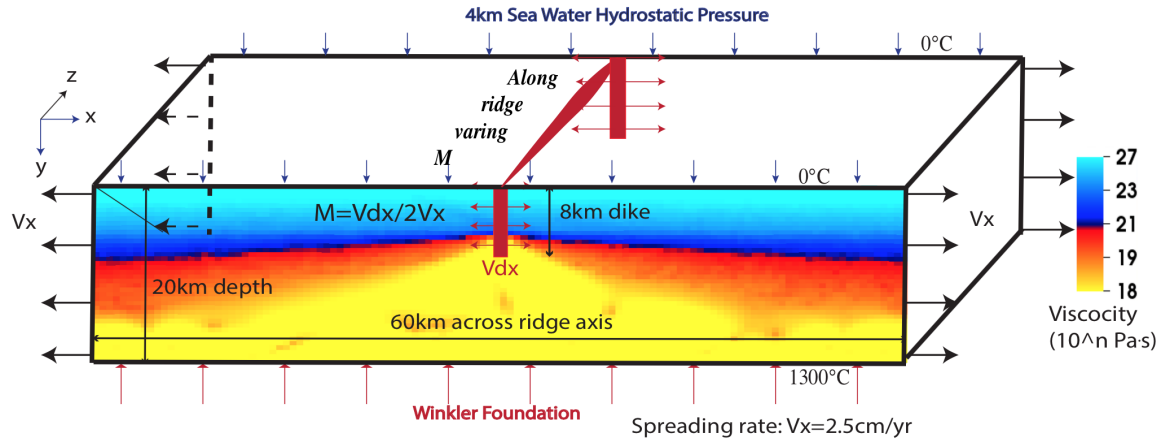


Figure 7: Model setup

## 2.3 Parameters to control

Although how to estimate the  $M$  values from observations has not been well established, we do have constraints from a large dataset of bathymetry, gravity and seismic surveys as

well as geological drilling. Generally, at slow spreading ridges, magma supplies mostly at the center of the ridge segment and decreases towards the end of the segment [Tolstoy et al., 1993, Chen and Lin, 1999]. There is also evidence for shorter wavelength of 10 to 20 km discrete focus of magma accretion along the ridge axis [Lin et al., 1990].

Based on these constraints, we can start considering only a few end-member scenarios of variations in M along the ridge axis. The variation in M is parametrized in terms of the functional forms (e.g. discrete increment, linear, sinusoidal and square root), its wavelength (e.g. 10km, 20km and 40km) and the ranges of M (e.g. 0.2 to 0.8, 0.5 to 0.7 and 0.5 to 0.8).

Preliminary pseudo-2D results show that the model behavior in faulting pattern is sensitive to the rate of strain weakening. Two cases of strain weakening are tested in this study. In one case (denoted as Type 1), cohesion linearly decreases from 44 MPa (denoted as  $Cohs_{init}$ ) to 4 MPa ( $Cohs_{end}$ ) for plastic strain accumulating from 0 ( $Plstrain_{init}$ ) to 0.1 ( $Plstrain_{end}$ ). It has a characteristic fault slip of 150 meters for Pseudo-2D models and 300 meters for 3D models. The other case (Type 2) assumes cohesion linearly decreasing from 44 MPa to 4 MPa for plastic strain accumulating from 0 to 0.33. In this case, the characteristic fault slip for Pseudo-2D models is 500 meters and for 3D models is 1km.

The characteristic fault slip  $F_{slip_c} = 3 \times dx \times Plstrain_{end}$  (3 is because the thickness of the shear bands is usually 2 to 4 times of the dx [Lavier et al., 2000]) means when  $F_{slip_c}$  amount of displacement takes place at the fault interface, the Cohesion of the material at the faulting interface will decrease to  $Cohs_{end}$ . In this way, under same amount of  $F_{slip_c}$ , models with different resolution should behave in the same way in terms of strain weakening and faulting patterns.

### 3 Results

*XT: choose some point in the model domain like Choi 2008 did, to monitor the values changes with time (e.g. stress for quantitatively analyzing the model behaviors)* Currently, we have three factors controlling the model behaviors. They are three ranges of M variation along the ridge axis (0.5~0.7; 0.5~0.8; 0.2~0.8), three functional forms of M variation (linear; sinusoidal; square root) and two types of weakening rate (Type 1 and Type 2) as mentioned in Parameters to control section. Generally, all models forms a median valley that deepens and widens toward the lower M side.

#### 3.1 Reference model description

We consider two models as our reference models: one, M varies linearly from 0.2 to 0.8 along the ridge axis; two, constant M along the ridge axis as a comparison to the varying M models.

### 3.1.1 M varies along the ridge axis

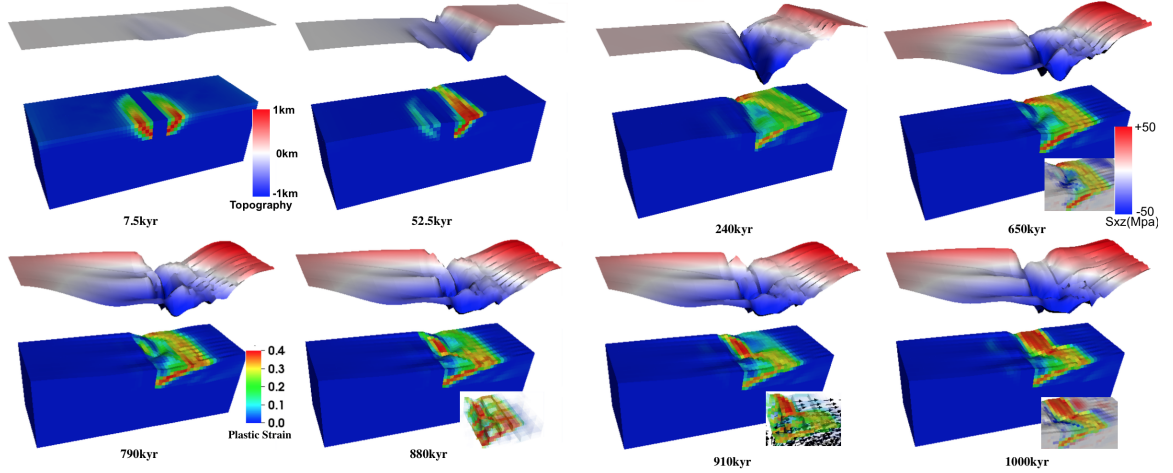


Figure 8: Reference model one: M linearly increases from 0.2 to 0.8 from front to back. The top layer is the topography of the model with five times vertical exaggeration. The green, yellow and red colors shown in the model domain are for Plastic strain. The number with kyr beneath is the time for the model with a unit of thousands of year. The two insets for 650kyr and 1000kyr is for shear stress  $\sigma_{xz}$  ( $Sxz$  in the figure). The inset for 880kyr is for plastic strain. The inset for 910kyr shows both plastic strain and the velocity vector.

*X<sup>T</sup>: remember to add description for rotation: low M side begin to fault and bend and nulate to high M side so that the faulting and bending is more or less simultaneous. Otherwise, it should be happening at different time.*

*In addition, the lowest topo point along the ridge is oblique firstly in a xz direction (why is it happening) and later as the secondary fault evolves, another shear topo low (show in the inset of 1000kyr) in -xz direction take place due to movement (show in the inset of 910kyr) of the hanging wall at  $M < 0.5$  side is to the -x while at  $M > 0.5$  side its footwall is moving to +x thus create this shear low. Two shear low make a X shape and a huge “corrugation” on the left hand side of the ridge-axis*

As shown in Figure 8, at 7.5kyr, high angle ( $\sim 60^\circ$  consistent with model parameter setup of frictional angle of  $30^\circ$ ) normal faults (shown as high plastic strain shear bands) begin to form near the ridge axis because the thickness of the crust is thinnest at the ridge center according to model thermal structure. They first initiate at the front (lower M side)

and then nucleate to the back (higher M side) because for each timestep, the tensional stress accumulates more at the lower M side and thus reach a yielding point earlier than higher M side. At 52.5kyr, the normal fault on the right hand side of the ridge axis continues to evolve while the one on the left becomes inactive. The choice of which fault will develop is a random event since the model setup is symmetrical across the ridge-axis. The timing difference of initiation of faulting along the ridge axis creates a constant offset in X-axis direction of breakways that the breakaway at the lower M side extends further than that of the higher M side. However, this offset will not increase because the velocity for the breakaway to move away from the axis is only controlled by the far field extension rate,  $V_x$ .

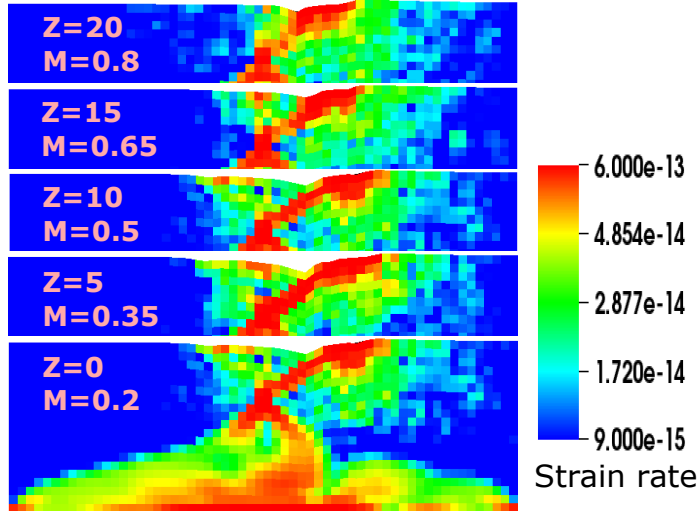


Figure 9: Strain rate at 107.5kyr with five slices along ridge axis(Z axis).

The location of the termination of the detachment fault where footwall begins to be exhumed to the surface varies along the ridge-axis (i.e. Z-axis). As shown in Figure 9, the highest strain rate regions can be interpreted as detachment fault interfaces. When  $M <= 0.5$ , although the fault displacement should be higher for lower M, the rate of bending of the fault has a maximum value controlled by the far field extension rate, thus the faulting interfaces are similar. When  $M > 0.5$ , the displacement as well as the amount of the bending of the fault decrease as M increases which help maintaining a higher angle fault and thus a nearer to the ridge-axis termination. However, this behavior is more or less compensated

by the hanging wall being pushed away from the ridge-axis due to excessive diking (when  $M > 0.5$ ). In a unit time, the volume of the exhumation is also smaller for the higher M side.

Corrugations are observed in the model since 240kyr. It will be further discussed in the discussion chapter. There are two contributing factors, for one, trans-extenstional stresses are created due to offset of the breakaway as well as the variation in fault displacements along the ridge axis; for the other, the variation of the position of the termination of the detachment fault might create anastomosing faults mentioned in [Smith et al., 2014].

The secondary near axis high angle normal fault is another common observation of the models. As shown in Figure 8, at the ridge axis with  $M > 0.5$  (i.e.  $Z > 10$ ), the existing normal fault will be pushed away from the ridge-axis due to excessive diking, as its mechanism has been mentioned in the introduction chapter, another new near axis normal fault is created at around 650kyr. As it evolve, the initial detachment fault become inactive (the transparent view of plastic strain shown in the rigth corner inset of time 880kyr). This secondary fault creates another dome and its composition is more likely to be volcanic rather than ultramafic, however, as it evolves, if it can last long, lower crust and upper mantle material can be exhumed to the surface. The composition of the domes observed at Kane magamullions is similar to this mechanism that ultramafic Babel dome is on the West and crustal inside-corner high on the East.

### 3.1.2 Constant M along the ridge axis

As shown in Figure 10, this constant M along the ridge-axis model create a median valley of  $\sim 20\text{km}$  in width and  $1 \sim 2\text{km}$  in depth which is similar to generally observation of Mid-Atlantic Ridges. The width and depth of the median valley is almost constant along the ridge-axis. The variation along the ridge-axis in breakaway and termination as well as the existence of corrugation mentioned in reference model one are not observed.

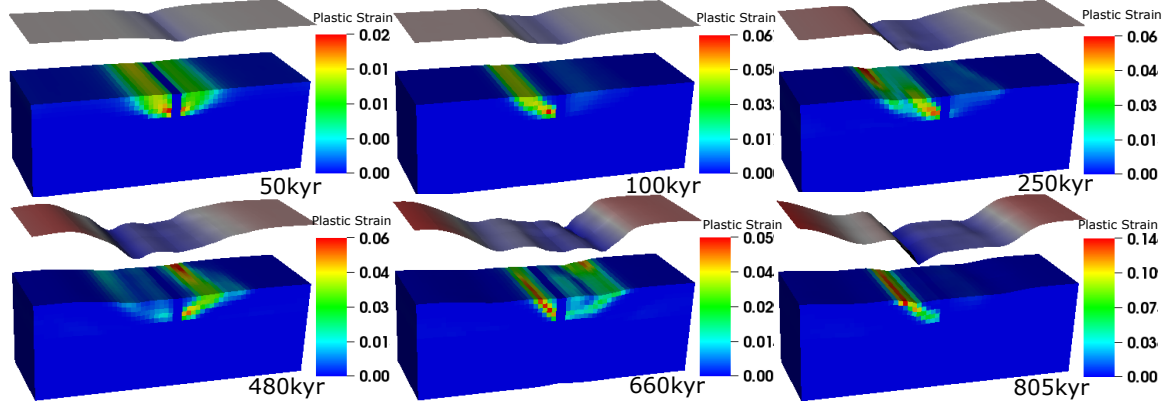


Figure 10: Reference model two: constant  $M = 0.8$  along the ridge-axis (i.e. Z axis). Type two weakening.

Based on the previous experience in pseudo-2D models or [Lavier et al., 2000], with higher characteristic fault displacement ( $3dx \times Pls_{end}$ ), Type two weakening compared with Type one weakening, the frequency of normal faulting alternation, for  $M > 0.5$  cases, is higher. However, interesting enough, when comparing pseudo-2D and 3D models when they are using Type two weakening under case of  $M = 0.8$ , even though the 3D Model has a larger  $F_{slip_c}$  of 1km than that of pseudo-2D model of 0.5kmr, 3D model has a lower frequency of faulting alternation.

### 3.2 Tables of all the data points

A	Alternating Fault	C	Corrugation	SL	Shear Topography Low
NA	Not Alternating	SF	Secondary Fault on one side	CB	Cut Back
DD	Double Dome	AM	Atlantis Massif		

Table 1: Model behaviors in short.

M range Weakening type	M28	M57	M58
Type one	NA; C; SL; SF <sub>1500 kyr</sub> ; DD	NA; C; SF <sub>1380 kyr</sub> ; CB <sub>330 kyr</sub> ; AM(opposite z)	
Type two			

Table 2: Linear functional form.

M range Weakening type	M28	M57	M58
Type one	NA; C; SL; SF <sub>995 kyr</sub>	NA; C; SL; SF <sub>760 kyr; 1320 kyr</sub> ; CB <sub>520 kyr</sub> ; AM	NA; C; SL; CB <sub>510 kyr</sub> ; SF <sub>760 kyr; 1140 kyr; 1990 kyr</sub>
Type two		NA; C; SL; SF <sub>680 kyr</sub> ; CB <sub>905 kyr</sub>	A <sub>450 kyr; 600 kyr</sub> ; C(only at low M); CB <sub>990 kyr</sub>

Table 3: Sinusoidal functional form.

M range Weakening type	M28	M57	M58
Type one	NA; C; SL; $CB_{205\text{kyr};330\text{kyr};1025\text{kyr}}$		NA; $C_{1770\text{kyr}}$ (due to shear with dif wave length); $SF_{860\text{kyr}}$ (high M); $SF_{1190\text{kyr}}$ (low M)(Dog Bone); $SF_{1690\text{kyr}}$
Type two		NA; C; $SF_{435\text{kyr};1060\text{kyr}}$ ; $CB_{585\text{kyr}}$ ; $CB_{735\text{kyr}}$ ; $CB_{910\text{kyr}}$ ; $CB_{970\text{kyr}}$	$A_{550\text{kyr};920\text{kyr}}$ ; C; $CB_{400\text{kyr}}$

Table 4: Square root functional form.

### 3.3 Fault Alternation

The fault alternation behavior observed in pseudo-2D models in cases  $M > 0.5$  is much more complicated in 3D models. The results shows that only Type two weakening with M58 will result in a alternating faulting pattern. *XT: integrate the area of  $M > 0.5$  with respect to Z to see if there is any quantatative analysis available.*

### 3.4 Variation of the range of M

### 3.5 Variation of the functional form

### 3.6 Influence of weakening rate

### 3.7 Summary of Findings

## **4 Discussion**

### **4.1 Discussion of Findings**

### **4.2 Influence of healing**

### **4.3 Model Limitation**

### **4.4 Reccommendation for Future Research**

## **5 Conclusions**

## References

- G. Baines, M. J. Cheadle, B. E. John, and J. J. Schwartz. The rate of oceanic detachment faulting at atlantis bank, sw indian ridge. *Earth and Planetary Science Letters*, 273(1-2):105–114, Aug. 2008. ISSN 0012821X. doi: 10.1016/j.epsl.2008.06.013.
- R. Buck, L. Lavier, and A. Poliakov. Modes of faulting at mid-ocean ridges. *Nature*, 434(7034):719–23, 2005. ISSN 1476-4687. doi: 10.1038/nature03358.
- Y. J. Chen and J. Lin. Mechanisms for the formation of ridge-axis topography at slow-spreading ridges: A lithospheric-plate flexural model. *Geophysical Journal International*, 136:8–18, 1999. ISSN 0956540X. doi: 10.1046/j.1365-246X.1999.00716.x.
- E. Choi, L. Lavier, and M. Gurnis. Thermomechanics of mid-ocean ridge segmentation. *Physics of the Earth and Planetary Interiors*, 171(1-4):374–386, Dec. 2008. ISSN 00319201. doi: 10.1016/j.pepi.2008.08.010.
- C. M. R. Fowler. *The solid earth: an introduction to global geophysics*. Cambridge University Press, 2004.
- S. Kirby and A. K. Kronenberg. Rheology of the lithosphere: Selected topics. *Reviews of Geophysics*, 25(6):1219–1244, 1987.
- L. L. Lavier, W. R. Buck, and A. N. B. Poliakov. Factors controlling normal fault offset in an ideal brittle layer. *Journal of Geophysical Research*, 105(B10):23431, 2000. doi: 10.1029/2000JB900108.
- J. Lin, G. M. Purdy, H. Schouten, J.-C. Sempere, and C. Zervas. Evidence from gravity data for focused magmatic accretion along the Mid-Atlantic Ridge. *Nature*, 344:627–632, 1990. ISSN 0028-0836. doi: 10.1038/344627a0.
- W. B. F. Ryan, S. M. Carbotte, J. O. Coplan, S. O’Hara, A. Melkonian, R. Arko, R. A. Weisel, V. Ferrini, A. Goodwillie, F. Nitsche, J. Bonczkowski, and R. Zemsky. Global multi-

resolution topography synthesis. *Geochemistry, Geophysics, Geosystems*, 10, 2009.  
ISSN 15252027. doi: 10.1029/2008GC002332.

D. K. Smith, H. Schouten, H. J. B. Dick, J. R. Cann, V. Salters, H. R. Marschall, F. Ji, D. Yoerger, A. Sanfilippo, R. Parnell-turner, C. Palmiotto, A. Zhelezov, H. Bai, W. Junkin, B. Urann, S. Dick, M. Sulanowska, P. Lemmond, and S. Curry. Development and evolution of detachment faulting along 50 km of the mid-atlantic ridge near 16.5°n. *Geochemistry Geophysics Geosystems*, pages 4692–4711, 2014. doi: 10.1002/2014GC005563.Received.

M. Tolstoy, A. J. Harding, and J. A. Orcutt. Crustal Thickness on the Mid-Atlantic Ridge: Bull's-Eye Gravity Anomalies and Focused Accretion. *Science*, 262(October):726–729, 1993. ISSN 0036-8075. doi: 10.1126/science.262.5134.726.

B. E. Tucholke, M. D. Behn, W. R. Buck, and J. Lin. Role of melt supply in oceanic detachment faulting and formation of megamullions. *Geology*, 36(6):455, 2008. ISSN 0091-7613. doi: 10.1130/G24639A.1.

D. L. Turcotte and G. Schubert. *Geodynamics*. Cambridge, 2002.